UBXN3B Restricts Viral Pathogenesis by Maintaining Hematopoietic Homeostasis

Tingting Geng [1*], Duomeng Yang [1*], Tao Lin [1], Andrew Harrison [1], Binsheng Wang [2], Blake Torrance [1], Long Yang [3], Laura Haynes [1], Gong Cheng[4], Anthony T. Vella [1], Erol Fikrig [5] and Penghua Wang [1#]

[1] Department of Immunology, School of Medicine, the University of Connecticut Health Center, Farmington, CT 06030, USA.

[2] Center on Aging and Department of Genetics and Genome Sciences, the University of Connecticut Health Center, Farmington, CT 06030, USA.

[3] School of integrative Medicine, Tianjin University of Traditional Chinese Medicine, Tianjin 301617, China.

[4] Department of Basic Sciences, School of Medicine, Tsinghua University, Beijing, China.

[5] Section of Infectious Diseases, Yale University School of Medicine, 333 Cedar Street, New Haven, CT, 06510, USA

* T.G. and D.Y contributed equally.

Address correspondence to: Penghua Wang, Ph.D., Department of Immunology, School of Medicine, University of Connecticut, UCONN Health, Farmington, CT 06030, USA. Email: pewang@uchc.edu, Tel: 860-679-6393.

Running title: UBXN3B regulates hematopoiesis

ABSTRACT

Hematopoiesis is finely regulated to enable timely production of the right number and type of mature immune cells to maintain tissue homeostasis. Dysregulated hematopoiesis may compromise antiviral immunity and/or exacerbate immunopathogenesis. Herein, we report an essential and new role of ubiquitin X domain containing gene 3B (UBXN3B) in balancing myelopoiesis and lymphopoiesis. *Ubxn3b* deficiency (*Ubxn3b*$^{-/-}$) results in a remarkable increase in myeloid cells and neutrophil-to-lymphocyte ratio, along with a reduction in lymphocytes in steady-state mice. This dysregulation is exacerbated during viral infection and renders mice highly vulnerable to severe lung pathology induced by severe acute respiratory syndrome coronavirus 2 and arthritis by arthritogenic alphaviruses. *Ubxn3b*$^{-/-}$ mice present normal type I IFNs, higher viral loads and inflammatory mediators, lower virus-specific immunoglobulin G and slower resolution of disease, when compared to *Ubxn3b*$^{+/+}$ littermates. Mechanistically, *Ubxn3b*$^{-/-}$ mice have fewer multipotent progenitors and common lymphoid progenitors, but more common myeloid progenitors. In particular, the precursor and immature B cell numbers are dramatically decreased in the bone marrow of *Ubxn3b*$^{-/-}$ mice. These data demonstrate that UBXN3B signaling is essential for restricting viral infection and immunopathogenesis by maintaining hematopoietic homeostasis.

Key word: hematopoiesis, UBXN, SARS-CoV-2, coronavirus, alphavirus, COVID-19.

INTRODUCTION

The immune system is comprised of various cell types that coordinate responses to infection by maintaining tissue and immune homeostasis. Peripheral immune cells, with the exception of a few cell types such as long-lived memory T cells and some tissue macrophages, are constantly replenished from bone marrow stem cells through progenitor cells [1]. For instance, approximately $0.5–1 \times 10^{11}$ granulocytes are generated daily in adult human individuals [2]. The hematopoietic system is a hierarchically organized, somatic stem cell-maintained organ system, with long-lived and self-renewing pluripotent hematopoietic stem cells (LT-HSCs) at its apex [1]. LT-HSCs differentiate into short-term multipotent progenitors (MPPs or ST-HSCs) and lineage-committed hematopoietic progenitors, which in turn will eventually differentiate into the numerous mature blood cell lineages [3]. While at the apex of the hematopoietic hierarchy, LT-HSCs are largely quiescent, and the highly proliferative MPPs are the primary contributor to steady-state hematopoiesis [4] [5]. MPPs are capable of differentiating into lineage-committed progenitors, e.g., common lymphoid progenitors (CLPs) and common myeloid progenitors (CMP), which turn into blast cells leading to specific cell types. These processes involve a global change of gene expression controlled by cell-intrinsic transcription factors and epigenetic modifiers, and cell-extrinsic factors such as cytokines, chemokines, growth factors, and interactions with osteoblasts, endothelial cells, reticular cells and stromal cells in its bone marrow niche [3]. The HSC differentiation cascade must be finely regulated to enable timely production of the right number and type of mature cells, i.e. homeostasis, disruption of which may lead to a pathological state, such as autoimmunity, immunodeficiency, cancer etc. As example, lymphopenia and a skewed myeloid-to-lymphoid ratio in the elderly may contribute to inflammaging and impaired immunity [6].

The human genome encodes 13 ubiquitin regulatory X (UBX) domain-containing proteins, designated UBXNs. The UBX domain shares weak homology with ubiquitin at the protein level and adopts the same three dimensional fold as ubiquitin[7]. A number of UBXNs

have been shown to bind multiple E3 ubiquitin ligases and an ATPase associated with various cellular activities (AAA ATPase), p97 [8,9]. We and other research groups have recently shown that several UBXNs regulate viral RNA-sensing RIG-I (retinoic acid inducible gene 1) like receptor -mitochondrial antiviral viral signaling (RLR-MAVS) [10-12] and Nuclear factor-κB (NF-κB) signaling pathways [13,14]. Of note, we recently reported that UBXN3B controlled DNA virus infection by positively regulating the dsDNA-sensing cGAS (cyclic di-GMP-AMP synthase)-STING (stimulator-of-interferon-genes) signaling and innate immunity [15]. However, the physiological function of UBXN3B in RNA virus infection remains unknown. To this end, we studied two positive-sense single-stranded RNA [(+) ssRNA] viruses of great public health significance, severe acute respiratory syndrome (COVID-19)-causing coronavirus 2 (SARS-CoV-2), and a mosquito-borne arthritogenic alphavirus, Chikungunya virus (CHIKV). Since its emergence in humans in China late 2019, SARS-CoV-2 has infected more than 112 million and killed over 2.5 million people worldwide (Source: World Health Organization, https://covid19.who.int), constituting the greatest global public health crisis in the 21st century. CHIKV is the causative agent of acute and chronic crippling arthralgia. The most recent CHIKV epidemic in the Americas has resulted in over 3 million infection cases in more than 40 countries (Source: Pan America Health Organization, www.paho.org). Although from very different families, both SARS-CoV-2 and CHIKV can elicit inflammatory responses and massive infiltration of immune cells into their target organs. CHIKV elicits self-perpetuating inflammation characterized by potent infiltration of macrophages, monocytes, neutrophils etc. into muscles and joints [16] [17]. SARS-CoV-2 induces life-threatening lung immunopathology, typified by elevated levels of inflammatory mediators, myeloid immune infiltrates in the lung, neutrophilia and lymphopenia [18]. Herein, we found that UBXN3B is essential for maintaining hematopoietic homeostasis. *Ubxn3b* deficiency (*Ubxn3b*$^{-/-}$) results in a systemic change in the steady-state immune cell composition, with a remarkable increase in myeloid cells, neutrophil-to-lymphocyte ratio (N/L), and a dramatic reduction in lymphocytes. This dysregulation is exacerbated during

viral infection and renders mice highly susceptible to severe lung pathology induced by SARS-CoV-2 and arthritis by arthritogenic alphaviruses. Mechanistically, UBXN3B is essential for maintaining MPPs and CLP homeostasis, precursor B cell differentiation and proliferation.

RESULTS

UBXN3B controls pathogenesis of respiratory viral diseases

Using a tamoxifen-inducible Cre-LoxP system, we recently successfully deleted global UBXN3B protein expression in adult mice and demonstrated that UBXN3B positively regulated the STING-mediated innate immune response to a DNA virus [15]. To understand the physiological function of UBXN3B in restricting pathogenesis of RNA viral diseases, we first tested respiratory viruses of public health significance including SARS-CoV-2. Because immunocompetent adult mice are minimally permissive to clinical isolates of SARS-CoV-2, we delivered human angiotensin-converting enzyme 2 (ACE2, the cellular entry receptor for SARS-CoV)-expressing Ad5 vector (replication-defective adenovirus vector) intranasally to the mouse lung before infection[19 20]. We observed a slight drop in body mass a few days post SARS-CoV-2 infection (p.i.) and rapid recovery of *Ubxn3b*$^{+/+}$ (Cre^{+} *Ubxn3b* $^{flox/flox}$) mice, while there was a ~10% reduction in body weight in *Ubxn3b*$^{-/-}$ (Cre^{+} *Ubxn3b* $^{flox/flox}$ treated with tamoxifen) littermates by days 3-4 p.i. and a significant delay in recovery (**Fig.1a**). Moreover, all infected *Ubxn3b*$^{-/-}$ mice showed hunched posture and decreased mobility on day 2 after infection, which was absent from *Ubxn3b*$^{+/+}$ animals (Supplemental Movie 1 and 2). Histopathological analyses by hematoxylin and eosin (H&E) staining revealed immune cell infiltrates in the lung of both *Ubxn3b*$^{+/+}$ and *Ubxn3b*$^{-/-}$ mice on day 3 p.i., compared to uninfected mice (Day 0). However, there was no significant difference in the numbers of immune infiltrates between the two genotypes (**Fig.1b**). On day 10 p.i. many clusters of brownish cells were noted in all *Ubxn3b*$^{-/-}$, but none in any *Ubxn3b*$^{+/+}$ mice (**Fig.1b**). We reasoned that these brownish cells in H&E

staining were representative of hemosiderosis, a form of iron overload disorder resulting in the accumulation of hemosiderin, an iron-storage complex. In the lung, macrophages phagocytose red blood cells due to vascular leakage, leading to iron overload. Using iron staining we tested this hypothesis and detected a few lightly iron-laden cells on day 3 p.i., but many clusters of heavily iron-laden cells by day 10 p.i. in all the *Ubxn3b*$^{-/-}$ lungs compared to *Ubxn3b*$^{+/+}$ (**Fig.1c, d**). On day 35 p.i., we still noted moderate lung hemosiderosis in some knockout mice. These data suggest an essential role of UBXN3B in restricting SARS-CoV-2 pathogenesis in the lung. We next asked if these observations could be extended to other respiratory viruses, such as influenza. Indeed, *Ubxn3b*$^{-/-}$ mice lost more body weight; and of note 70% of them succumbed to a dose of H1N1 influenza A that was sublethal to *Ubxn3b*$^{+/+}$ mice (**Fig.1e, f**).

Severe COVID-19 pathogenesis is a combination of a direct cytopathic effect of SARS-CoV-2 replication and hyper-inflammation in the lung [18]. In particular, COVID-19 fatality is strongly associated with elevated inflammatory mediators (interleukin 6 IL-6, tumor necrosis factor TNF-α etc.) [18]. We first examined viral loads and immune gene expression. The viral loads in the lungs were higher in *Ubxn3b*$^{-/-}$ when compared to *Ubxn3b*$^{+/+}$ mice on day 3 p.i, and by day 10 p.i. virus was almost cleared (**Fig.2a**). The serum cytokines IL-6, TNF-α, IL-10 and GM-CSF were higher in *Ubxn3b*$^{-/-}$ than in *Ubxn3b*$^{+/+}$ on day 3 p.i. (**Fig.2b**), which is consistent with clinical observations in severe COVID-19 patients. The concentrations of serum IFN-α, CXCL10 and IFN-γ were modestly upregulated, but equally in both *Ubxn3b*$^{-/-}$ and *Ubxn3b*$^{+/+}$ mice after SARS-CoV-2 infection, suggesting a normal type I/II IFN response (**Fig.2b**).

COVID-19 fatality is strongly associated with an imbalance in immune cell compartmentalization, characterized by neutrophilia and lymphopenia [21 22 23 24 25 26]. We analyzed neutrophils and T cells in the lung by flow cytometry and found that the total CD45^{+} immune cell counts per lung were ~10-fold higher in SARS-CoV-2-infected animals than mock-treated animals. However, there was no significant difference between *Ubxn3b*$^{-/-}$ and *Ubxn3b*$^{+/+}$ littermates (**Fig.3a**). Upon close examination we detected ~3 –fold increase in *Ubxn3b*$^{-/-}$

compared to *Ubxn3b*$^{+/+}$ mice in the frequency of CD11b^{+} cells, while total and CD4^{+} T cells were reduced in *Ubxn3b*$^{-/-}$ (**Fig.3b**). Importantly, the ratio of neutrophil-to-T lymphocytes (N/L) in the lung was significantly higher (3.2-fold) in *Ubxn3b*$^{-/-}$ (**Fig.3c**), which is consistent with clinical observations in severe COVID-19 patients [27]. This prompted us to examine more immune cell populations in the lung and peripheral blood, and the longer impact of SARS-CoV-2 infection on immune cells. We noted ~3-fold increase in neutrophil and 10-fold decrease in B cell frequencies (**Fig.3d,** Supplemental **Fig.1**); the N/L ratio was also much higher in the blood of *Ubxn3b*$^{-/-}$ than *Ubxn3b*$^{+/+}$ mice on day 3 p.i. (**Fig.3e**). By day 35 p.i., lower total immune cells per lung in *Ubxn3b*$^{-/-}$ than *Ubxn3b*$^{+/+}$ mice were observed, however, more myeloid cells such as neutrophils and macrophages/monocytes, a higher N/L ratio, but fewer B and T lymphoid cells in *Ubxn3b*$^{-/-}$ (**Fig.3f, g**). Of note, the B cell frequency were most dramatically decreased (5-20-fold) in both the lung and blood (**Fig.3f, g**). Consistently, there were ~40% fewer total CD45^{+} cells in the blood (**Fig.3h**) and lymphocytes in the marginal zone of the white pulp marked by greater myeloid infiltrates in the red pulp in the spleen of *Ubxn3b*$^{-/-}$ than in *Ubxn3b*$^{+/+}$ on day 35 p.i. (Supplemental **Fig.2**).

UBXN3B controls pathogenesis of alphaviral arthritis

The aforementioned results demonstrate a profound change in the immune cell compartmentalization in *Ubxn3b*$^{-/-}$ during SARS-CoV-2 infection, characterized by much greater myeloid and fewer lymphoid cells. We then asked if this phenotype could be extended to other viral diseases in the absence of *Ubxn3b*. Although from very different families, both SARS-CoV-2 and CHIKV, an arthritogenic alphavirus, can elicit inflammatory cytokines and massive infiltration of immune cells into their target organs. CHIKV was directly injected into one footpad to induce swelling and acute arthritis in mice. Cre^{+} *Ubxn3b* $^{flox/flox}$ (*Ubxn3b*$^{+/+}$) and tamoxifen-treated Cre^{-} *Ubxn3b* $^{flox/flox}$ (wild-type) mice showed progressive footpad swelling, which peaked on day 6 p.i. and receded rapidly. In contrast, tamoxifen-treated Cre^{+} *Ubxn3b* $^{flox/flox}$ (*Ubxn3b*$^{-/-}$)

mice presented more severe and persistent foot swelling (**Fig.4a, b**). Histopathological analyses by H&E staining confirmed increased immune cell infiltration into the muscles and joints of *Ubxn3b*$^{-/-}$ compared to *Ubxn3*$^{+/+}$ littermates on day 16 p.i. (**Fig.4c, d**). Similar results were observed for another arthritogenic alphavirus, O'nyong nyong (ONNV) (Supplemental **Fig.3**). Moreover, the CHIKV viremia on days 2 and 4 p.i., and viral loads in footpads on days 4 and 8 p.i. were significantly higher in *Ubxn3b*$^{-/-}$ than *Ubxn3*$^{+/+}$ mice (Supplemental **Fig.4**). Next the concentrations of serum immune mediators by multiplex ELISA were assessed, and higher levels of IL-6, CXCL10, TNF-α and IFN-γ with different kinetics were observed in *Ubxn3b*$^{-/-}$ over *Ubxn3b*$^{+/+}$ mice, in particular, even after viremia had been cleared on day 8 p.i (Supplemental **Fig.5**). We detected more neutrophils and macrophages/monocytes, but fewer B and T cells in CHIKV-targeted tissues, e.g. the footpad, blood and spleen of *Ubxn3b*$^{-/-}$ than *Ubxn3b*$^{+/+}$ mice (**Fig.4e**). Of note, the N/L ratios were much higher in all the tissue of *Ubxn3b*$^{-/-}$ mice (**Fig.4fe**). These data suggest that UBXN3B signaling is essential for not only clearing CHIKV rapidly but also restraining immunopathology post viral clearance.

Because B/T lymphocyte counts were significantly reduced in *Ubxn3b*$^{-/-}$, we asked if this deficiency influenced production of virus-specific antibodies. Indeed, the concentrations of serum anti-CHIKV/ONNV/influenza immunoglobulin G (IgG) were ~50% lower in *Ubxn3b*$^{-/-}$ than in *Ubxn3b*$^{+/+}$ mice (Supplemental **Fig.6**).

UBXN3B regulates steady-state hematopoietic homeostasis

These results suggest an essential role of UBXN3B in maintenance of immune cell homeostasis during viral infection regardless of viral species. Therefore, to test the hypothesis that dysregulated immune homeostasis is caused by *Ubxn3b*$^{-/-}$ deficiency, we reasoned that in the steady state *Ubxn3b*$^{-/-}$ mice should have alterations that cannot be explained by infection. Indeed, by flow cytometry, we observed a significant increase in the frequencies of myeloid cells (neutrophils, monocytes, macrophages), in the blood and spleen of *Ubxn3b*$^{-/-}$ compared to

Ubxn3b$^{+/+}$ mice. Although the T cell frequencies were slightly lower, its counts were significantly lower in both tissues of *Ubxn3b*$^{-/-}$ (**Fig.5a, b**). The total CD45^{+} count per spleen was ~3-fold lower in *Ubxn3b*$^{-/-}$ (**Fig.5b**). Of note, *Ubxn3b*$^{-/-}$ mice had over 10 times lower B cell counts and frequencies in both tissues of knockout mice (**Fig.5a, b**). Although the magnitudes of difference in each immune cell frequency and count varied with tissues, the N/L ratios were uniformly much higher in all tissues of *Ubxn3b*$^{-/-}$ when compared to *Ubxn3b*$^{+/+}$ mice (**Fig.5a, b**).

These results suggested that UBXN3B regulates hematopoietic homeostasis. To this end, we first quantitated mature immune cells in the bone marrow. Among all live cells (after lysis of red blood cells), neutrophils were most abundant, then B cells. Consistent with observations in the peripheral immune organs, the frequency of neutrophils was significantly greater, while the number of B cells was ~6-fold lower in *Ubxn3b*$^{-/-}$ than in *Ubxn3b*$^{+/+}$ mice (**Fig.6a, b**). These results suggest that elevated N/L ratios in *Ubxn3b*$^{-/-}$ is due to dysregulated hematopoiesis, which we tested by assessing bone marrow stem cells and progenitors. Total HSCs (Lin^{-} Sca^{+} Kit^{+}) contains two populations, long-term HSCs, which are capable of self-renewal but are quiescent at steady state, and short-term multipotent HSCs (also known as MPPs), which are capable of differentiating into lineage-committed progenitors. We noted that there were fewer total HSCs in *Ubxn3b*$^{-/-}$ when compared to *Ubxn3b*$^{+/+}$; this was because of a decrease in MPPs, but not LT-HSCs, which were the same (**Fig.6c, d**). The frequency of lineage-committed common lymphoid progenitors (CLPs) was also reduced, while the common myeloid progenitors (CMPs) trended higher in *Ubxn3b*$^{-/-}$. Remarkably, the B cell precursors (Pre-B) and immature B cells were significantly lower in *Ubxn3b*$^{-/-}$ (**Fig.6c, d**).

DISCUSSION

UBXN3B might participate in diverse cellular activities, ranging from lipid metabolism [28,29,30,28,31] [32-35], protein degradation [36,37], mRNA stability [38], protein translocation [39] to regulation of innate

immunity [15]. In this study, we discovered a novel physiological function of UBXN3B in hematopoietic hemostasis with subsequent control of immunopathogenesis during viral infection. These multifaceted functions of UBXN3B are likely attributable to its capability as an adaptor to interface different E3 ligases and substrates [10] under different physiological conditions and developmental stages. The involvement of an adaptor in an E3 ligase action could greatly expand the substrate spectrum of the E3 ligase in response to various physiological and environmental cues. Our conclusion is substantiated by several pieces of evidence. First, *Ubxn3b*$^{-/-}$ mice presented worse lung damage during SARS-CoV-2 infection and arthritis elicited by arthritogenic alphaviruses than *Ubxn3b*$^{+/+}$ mice. Second, *Ubxn3b*$^{-/-}$ mice had higher viral loads and inflammatory mediators such as IL-6 and TNF-α. Third, lymphocytes, in particular the B cell numbers were significantly lower, while neutrophils and monocytes/macrophages were greater in various *Ubxn3b*$^{-/-}$ organs during the steady state and viral infection. Fourth, production of the virus-specific IgG was impaired in *Ubxn3b*$^{-/-}$ mice. Mechanistically, UBXN3B might control RNA virus infection by regulating STING [15] [40]. However, steady-state hematopoiesis was normal in *Sting*-deficient mice [41], suggesting that the primary function of UBXN3B during RNA virus infection is independent of STING. Furthermore, expression of type I IFNs was normal in *Ubxn3b*$^{-/-}$ mice. These data suggest that dysregulated hematopoiesis may be the main contributor to failure of viral clearance and prolonged immunopathology in *Ubxn3b*$^{-/-}$ mice. Indeed, the fine balance between lymphopoiesis and myelopoiesis was interrupted, characterized by more CMPs and neutrophils, and fewer CLPs and B cells in the *Ubxn3b*$^{-/-}$ bone marrow. In particular, proliferation of precursor B cells was significantly inhibited in the *Ubxn3b*$^{-/-}$ bone marrow, suggesting that UBXN3B play an important role in transition of progenitor B to precursor B cells.

Although belonging to very different families of RNA viruses, both arthritogenic alphaviruses and SARS-CoV-2 elicit immunopathology in their target tissues, including massive immune infiltrates and elevated levels of systemic pro-inflammatory mediators [16] [17] [18]. In

particular, COVID-19 fatality is strongly associated with neutrophilia and lymphopenia [18], which was partly recapitulated in *Ubxn3b*$^{-/-}$ mice. These animals were typified by neutrophilia and lymphopenia during steady state and viral infection, were highly prone to vascular damage by SARS-CoV-2 in the lung, and were slow to recover from infection. Similarly, viral clearance and resolution of arthritis elicited by alphaviruses was significantly delayed in *Ubxn3b*$^{-/-}$ mice. This was not due to type I IFNs, which were normal in *Ubxn3b*$^{-/-}$ mice; rather likely because of a reduction in B/T cell numbers and consequently virus-specific antibody production. Indeed, T lymphopenia is associated with shortened survival independently of and /or additive to traditional risk factors, especially when accompanied by heightened inflammation in general adults [42]. Primary B-cell immunodeficiency may lead to a defective production of antigen-specific antibodies and predisposition to recurrent and severe infections [43] and frequently autoimmune diseases [44]. On the other hand, heightened immunopathology and tissue damage persisted in *Ubxn3b*$^{-/-}$ mice even after viral clearance (day 16 post CHIKV, day 10 post SARS-CoV-2 inoculation), suggesting that UBXN3B controls immunopathogenesis disassociated from viral replication. Indeed, chronic CHIKV arthritis pathogenesis can progress without active viral replication [45]. The hyperinflammation phase of COVID-19 generally happens after viral load peak, with a few infectious viral particles [46]. At the post viral clearance stage, a high N/L ratio may underlie sustained inflammation. Indeed, high N/L ratios are correlated with poor prognosis of severe COVID-19 patients [47 27]. The N/L ratio is also the most reliable biomarkers associated with numerous chronic inflammatory diseases, such as type II diabetes [48], cardiovascular disease [49], aging [50] etc., which are significant risk factors for COVID-19 mortality [18]. These conditions are characterized by a low-grade pro-inflammatory and an “immunosenescence”-like immune state that is unable to clear viruses [27]. In this regard, UBXN3B deficiency might resemble the aging immune state, which is prone to viral infection and chronic inflammatory conditions. The protective role of UBXN3B in these disease conditions in mice may be potentially applicable to those in humans considering that the UBXN3B protein is highly

283 conserved in mammals (98% identity between human and rodent protein). Importantly, an
284 rs374702773 (delta T allele in intron) in UBXN3B is associated with protection against alcoholic
285 liver cirrhosis, a chronic inflammatory condition in humans [51].

286 In summary, our results suggest that a high N/L ratio predisposes an individual to
287 persistently heightened immunopathogy during viral infection that can lead to damaging organ
288 inflammation. Immediate future work will pinpoint the molecular mechanism of UBXN3B action
289 in immune progenitors and function of UBXN3B in auto-inflammatory diseases.

MATERIALS AND METHODS

Mouse model

The mouse line with the exon 1 of Ubxn3b flanked by two LoxP sites (Ubxn3b$^{flox/flox}$) were generated via homologous recombination by Dr. Fujimoto at Nagoya University [32]. The homozygous Ubxn3b$^{flox/flox}$ were then crossed with homozygous tamoxifen-inducible Cre recombinase-estrogen receptor T2 mice (The Jackson Laboratory, Stock # 008463) to generate Cre^{+} *Ubxn3b*$^{flox/flox}$ littermates. To induce Ubxn3b deletion, > 6-weeks old mice were injected with 100 µl of tamoxifen (10 mg / ml in corn oil) (Sigma, #T5648) via intraperitoneal (i.p.) every 2 days for a total duration of 8 days (4 doses). Successful deletion of Ubxn3b was confirmed in our recent study [12]. A half of Cre^{+} *Ubxn3b*$^{flox/flox}$ litters were treated with tamoxifen and designated *Ubxn3b*$^{-/-}$; the other half were treated with corn oil only and designated *Ubxn3b*$^{+/+}$. Mice were allowed to purge tamoxifen for at least 4 weeks before any infection or analyses was performed. The animal protocols were approved by the Institutional Animal Care and Use Committee at the University of Connecticut and Yale University.

Antibodies, Cell lines and Viruses

Human embryonic kidney 293 cells transformed with T antigen of SV40 (HEK293T, # CRL-3216) and Vero cells (monkey kidney epithelial cells, # CCL-81) were purchased from American Type Culture Collection (ATCC) (Manassas, VA20110, USA). These cell lines are not listed in the database of commonly misidentified cell lines maintained by ICLAC. Cells were grown in DMEM supplemented with 10% fetal bovine serum (FBS) and antibiotics/antimycotics (Life Technologies, Grand Island, NY 14072 USA).We routinely added MycoZAP (Lonza Group, Basel, Switzerland) to cell cultures prevent mycoplasma contamination.

SARS-CoV-2 (NR-52281, Isolate USA-WA1/2020) was provided by BEI Resources (funded by National Institute of Allergy and Infectious Diseases and managed by ATCC, United

States). The CHIKV French La Reunion strain LR2006-OPY1 was a kind gift of the Connecticut Agricultural Experiment Station at New Haven, CT, USA. The CHIKV vaccine strain 181, clone 25 was recovered from a plasmid and used for enzyme-Linked Immunosorbent assay (ELISA) [52] [53]. The ONNV UgMP30 strain (NR-51661) was provided by BEI Resources. All these viruses were propagated in Vero cells. The full-length human ACE2 [Accession No: NM_021804.2] cDNA was inserted into pAV-EGFP-CMV/FLAG and Ad5 viruses were prepared by Vector Builder Inc. (Chicago, IL 60609, USA).

Concentration of SARS-CoV-2

The virus was grown in Vero cells for 72hrs, and the culture medium was cleared by brief centrifugation. A PEG-it Virus Precipitation Solution (Cat# LV810A-1, System Biosciences, Palo Alto, CA 94303, USA) was added to 40ml of virus culture at a 1:4 ratio, incubated overnight at 4°C. The mixture was centrifuged at 1500xg for 30 min, and the resulting pellet was suspended in 1ml of DMEM medium. In parallel, Vero cell culture medium without virus was processed in the same way and used for mock infection.

Plaque-Forming Assay

Quantification of infectious viral particles in sera or homogenized tissues was performed on Vero cell monolayer [54]. Briefly, viral samples were incubated with confluent Vero cells (6-well plate) at 37□°C for 2□hr. The inoculum was then removed and replaced with 2□ml of DMEM complete medium with 1% SeaPlaque agarose (Cat.# 50100, Lonza). The cells were incubated at 37□°C, 5% CO_2 for 3 days, and on the fourth day the cells were stained with Neutral Red (Sigma-Aldrich) overnight.

Mouse Infection and Monitoring

Mice were administered intranasally $2x10^8$ plaque forming units (PFU) of Ad5-hACE2, after 5 days then intranasally inoculated with $2x10^5$ PFU of SARS-CoV-2 or mock. The body mass of individual mice was weighed on the day of infection (Day 0) as a baseline. The percentage change in an animal was calculated as 100 x (Day n-Day 0)/Day 0, where n defines the length of infection (in days).

About 3×10^5 plague-forming units (PFU) of CHIKV LR2006-OPY1 or ONNV was inoculated at the ventral side of a hind foot subcutaneously. The thickness and width of the perimetatarsal area of the hind foot were measured using a precision metric caliper. The foot dimension was calculated as width × thickness, and the results were expressed as fold increase in the foot dimension after infection compared to before infection (day 0 baseline).

Tissue Histology

Tissues were fixed in 4% paraformaldehyde (PFA), embedded in paraffin, cut into 4µM- thick sections, immobilized to glass slides, decalcified, and processed for hematoxylin and eosin staining. Arbitrary arthritic disease scores (on a 1–5 scale with 1 being the slightest, 5 the worst) were assessed using a combination of histological parameters, including exudation of fibrin and inflammatory cells into the joints, alteration in the thickness of tendons or ligament sheaths, and hypertrophy and hyperlexia of the synovium[21] in a double-blinded manner.

Hemosiderosis was evaluated by iron staining (Prussian Blue stain) (Cat. # ab150674, from Abcam, Cambridge, CB2 0AX, UK). Lungs were fixed in 4% PFA, embedded in paraffin, cut into 4µM- thick sections, immobilized to glass slides, deparaffinized in xylene, rinsed with 100% ethanol, hydrated progressively in 95%, 70% ethanol and distilled water. The slides were incubated in Iron Stain Solution (1:1 of potassium ferrocyanide solution to hydrochloric acid solution) for 3 min at ambient temperature, rinsed thoroughly in distilled water, stained in Nuclear Fast Red Solution for 5 minutes, rinsed again with distilled water 4 times, dehydrated in 95% alcohol followed by absolute alcohol, and finally mounted in synthetic resin. The slides

were assessed with an Accu-Scope microscope EXI-310 and images were acquired by an Infinity II camera and software.

Reverse Transcription and Quantitative (q) PCR

Up to 1□×□10^6 cells or 10mg, tissues were collected in 350□µl of RLT buffer (QIAGEN RNeasy Mini Kit). RNA was extracted following the QIAGEN RNeasy manufacturer's instructions. Reverse transcription of RNA into complementary DNA (cDNA) was performed using the BIO-RAD iScript™ cDNA Synthesis Kit. Quantitative PCR (qPCR) was performed with gene-specific primers and SYBR Green PCR master mix. Results were calculated using the –ΔΔCt method and a housekeeping gene, beta actin, as an internal control. The qPCR primers and probes for immune genes were reported in our previous studies [15, 40,55]. The primers for SARS-CoV-2 were forward: 5'-GAC CCC AAA ATC AGC GAA AT-3' and reverse: 5'-TCT GGT TAC TGC CAG TTG AAT CTG-3', CHIKV forward: 5′-GCGAATTCGGCGCAGCACCAAGGACAACTTCA-3′ and reverse 5′-AATGCGGCCGCCTAGCAGCATATTAGGCTAAGCAGG-3′, ONNV forward primer: 5′-GCAGGGAGGCCAGGACAGT-3' and reverse 5′-GCCCCTTTTTCYTTGAGCCAGTA-3′.

Fluorescence-Activated Cell Sorting (FACS)

FACS was performed according to our published study [17]. Mouse tissues were minced with a fine scissor and digested in 4 mL of digestion medium [20 mg/mL collagenase IV (Sigma-Aldrich, St. Louis, MO, USA), 5 U/mL dispase (Stemcell, Cambridge, MA, USA), and 50 mg/mL DNase I mix (Qiagen, Germantown, MD, USA) in complete RPMI1640 medium] at 37 °C for 4 hrs. The lysate was filtrated with a 40µm cell strainer. Cells were then pelleted down by centrifugation at 500 × g for 5 min. The red blood cells in the cell pellet were lysed three times with a lysis buffer (Cat. # 420301 from BioLegend, San Diego, CA 92121, USA). Cells were suspended in FACS

buffer and stained for 30 min at 4 °C with the desired antibody cocktails (Biolegend, San Diego, CA, US) of APC-Fire 750-anti CD11b (Cat. # 101261, clone M1/70), Alexa Fluor 700-anti Ly-6G (Cat. # 127621, clone 1A8), Brilliant Violet 421-anti CD11c (Cat. # 117343, clone N418), PerCP-Cy5.5-anti MHC II (Cat. # 107625, clone M5/114.15.2), PE-anti Tetherin (PCDA1) (Cat. # 12703, clone 10C2), Brilliant Violet 510-anti F4/80 (Cat. # 123135, clone BM8), APC-anti CD68 (Cat. # 137007, clone FA-11), PE-Dazzle 594-anti CD3 epsilon (Cat. # 100347, clone 145-2C11), Brilliant Violet 711-anti CD4 (Cat. # 100557, clone RM4-5), Brilliant Violet 570-anti CD8a (Cat. # 100739, clone 53-6.7), Brilliant Violet 650 anti-CD161 (NK1.1) (Cat. # 108735, clone PK136), FITC anti-CD117 (cKit) (Cat. # 105805, clone 2B8), PE anti- erythroid cells (Cat. # 116207, clone TER-119), Brilliant Violet 711-anti CD115 (Cat. # 135515, clone AFS98), FITC-anti CD25 (Cat. # 102005, clone PC61), Zombie UV (Cat. # 423107), PE-Cy7-anti CD45 (Cat. # 103113, clone 30-F11), TruStain FcX-anti CD16/32 (Cat. # 101319, clone 93), APC anti-CD127 (IL-7Ra) (Cat. # 135011, clone A7R34), PE-Dazzle 594 anti-Sca-1 (Ly-6A/6E) (Cat. # 108137, clone D7), PE-Cy5 anti-Flt-3 (CD135) (Cat. # 135311, clone A2F10), Brilliant Violet 421-anti CD34 (Cat. # 119321, clone MEC14.7), PE anti-CD16/32 (Cat. # 101307, clone 93), Brilliant Violet 711-anti IgM (Cat. # 406539, clone RMM-1), Brilliant Violet 421-anti CD45R (B220) (Cat. # 103239, clone RA3-6B2), Alexa Fluor 700-anti CD19 (Cat. # 115527, clone 6D5), PE-Cy7 anti-CD93 (Cat. # 136505, clone AA4.1) and Lin- (anti-CD4, CD8, CD11b, Cd11c, Gr1, NK1.1, TER119, Singlec-F, FceRIa, CD19, B220 cocktail). After staining and washing, the cells were fixed with 4% PFA and analyzed on a Becton-Dickinson FACS ARIA II, CyAn advanced digital processor (ADP). Data were analyzed using the FlowJo software. Among $CD45^+$ cells, $CD11b^+$ $Ly6G^+$ cells were classified as neutrophils, $Ly6G^-CD11b^+$ $F4/80^+$ as monocytes/macrophages, $Ly6G^-$ $CD11b^+$ $CD115^+$ as monocytes, $Ly6G^-$ $CD11c^+$ MHC II^+ as dendritic cells (DC), $CD3^+$ as total T cells, $CD3^+$ $CD4^+$ as CD4 T cells, $CD3^+$ $CD8^+$ as CD8 T cells, $CD19^+$ as B cells. Lin^- Sca^+ Kit^+ cells were identified as total HSCs, which were subdivided into $Flt3^{high}$ (short-term HSC or MPP) and $Flt3^{low}$ (long-term HSC). Lin^- Sca^- Kit^+ cells were subdivided into $CD34^{low}$ $CD16/32^{low}$ (MEP),

418 $CD34^{high}$ $CD16/32^{low}$ (CMP) and $CD34^{low}$ $CD16/32^{high}$ (GMP). The Lin^{-} $CD127^{+}$ Kit^{+} cells were
419 identified as CLP.
420
421 *Multiplex Enzyme-Linked ImmunoSorbent Assay (ELISA)*
422 We used a LEGENDPlex (Biolegend, San Diego, CA 92121, USA) bead-based immunoassay to
423 quantify the cytokine concentrations in the cell culture supernatant of SARS-CoV-2 infected
424 cells. The procedures were exactly the same as in the product manual. Briefly, the supernatants
425 or standards were mixed with antibody-coated microbeads in a filter-bottom microplate, and
426 incubated at room temperature for 2hrs with vigorous shaking at 500 rpm. After removal of
427 unbound analytes and two washes, 25 µL of detection antibodies were added to each well, and
428 the plate was incubated at room temperature for 1hr with vigorous shaking at 500 rpm. 25 µL of
429 SA-PE reagent was then added directly to each well, and the plate was incubated at room
430 temperature for 30min with vigorous shaking at 500 rpm. The beads were washed twice with
431 wash buffer, and then transferred to a microfuge tube. The beads were fixed with 4% PFA for
432 15min and resuspended in the assay buffer. The beads were run through a BIORAD ZE5 and
433 the concentrations of analytes were calculated with the standards included using the
434 LEGENDPlex software.
435
436 *Quantification of IgG by Enzyme-Linked ImmunoSorbent Assay (ELISA)*
437 One nanogram of recombinant SARS-CoV-2 Spike protein, ~$1x10^{6}$ viral particles in coating
438 buffer (0.05 M carbonate-bicarbonate, pH 9.6), or recombinant A/PR/8/34 influenza NP
439 (generated by UConn Health Protein Expression Core) was coated to a 96-well microplate at
440 4°C overnight. The plate was washed once with wash solution (50 mM Tris, 0.14 M NaCl, 0.05%
441 Tween 20, pH 8.0), and blocked with 4% bovine serum albumin at room temperature for 2hrs.
442 100µL of each diluted serum (500-fold) was added a well and incubated at room temperature for
443 1hr, then washed three times. 100µL of diluted horseradish peroxidase-conjugated goat anti-

mouse IgG was added to each well and incubated at room temperature for 1hr. After stringency wash, 100µL of substrate 3,3',5,5' - tetramethylbenzidine (TMB) was added to each well and incubated at room temperature for 5-30min for color development, and terminated by 100µL of 0.16M sulfuric acid. The absorption at wavelength 450nm (A_{450nm}) was read on a Cytation 1 plate reader (BioTek, Winooski, VT, USA).

Data Acquisition and Statistical Analysis

The sample size chosen for our animal experiments in this study was estimated according to our prior experience in similar sets of experiments and power analysis calculations (http://isogenic.info/html/power_analysis.html). All animal results were included and no method of randomization was applied. All data were analyzed with a GraphPad Prism software by non-parametric Mann-Whitney test or two-tailed Student's *t*-test depending on the data distribution. The survival curves were analyzed by Log-Rank test. P values of ≤0.05 were considered statistically significant.

459 **Footnotes**

460

461 Author contribution: T.G designed and performed the majority of the experimental procedures
462 and data analyses. D.Y., T.L., A.G.H. and L.Y. contributed to some of the experimental
463 procedures and/or provided technical support. B.W. contributed to some FACS analyses. B.T.
464 and L.H. helped to acquire the influenza data. G.C., A.T.V. and E.F. helped with data
465 interpretations. P.W. conceived and oversaw the study. T.G. and P.W. wrote the paper and all
466 the authors reviewed and/or modified the manuscript.

467

468 Funding Source: This project was funded in part by National Institutes of Health grants to P. W,
469 R01AI132526 and R21AI155820.

470

471 Conflict of Interest: No financial or non-financial interest to disclose.

472

473

474

References

1 Boettcher, S. & Manz, M. G. Regulation of Inflammation- and Infection-Driven Hematopoiesis. *Trends Immunol* **38**, 345-357, doi:10.1016/j.it.2017.01.004 (2017).

2 Dancey, J. T., Deubelbeiss, K. A., Harker, L. A. & Finch, C. A. Neutrophil kinetics in man. *J Clin Invest* **58**, 705-715, doi:10.1172/JCI108517 (1976).

3 Rieger, M. A. & Schroeder, T. Hematopoiesis. *Cold Spring Harb Perspect Biol* **4**, doi:10.1101/cshperspect.a008250 (2012).

4 Busch, K. *et al.* Fundamental properties of unperturbed haematopoiesis from stem cells in vivo. *Nature* **518**, 542-546, doi:10.1038/nature14242 (2015).

5 Rodriguez-Fraticelli, A. E. *et al.* Clonal analysis of lineage fate in native haematopoiesis. *Nature* **553**, 212-216, doi:10.1038/nature25168 (2018).

6 Groarke, E. M. & Young, N. S. Aging and Hematopoiesis. *Clin Geriatr Med* **35**, 285-293, doi:10.1016/j.cger.2019.03.001 (2019).

7 Schuberth, C. & Buchberger, A. UBX domain proteins: major regulators of the AAA ATPase Cdc48/p97. *Cell Mol Life Sci* **65**, 2360-2371 (2008).

8 Kondo, H. *et al.* p47 is a cofactor for p97-mediated membrane fusion. *Nature* **388**, 75-78 (1997).

9 Alexandru, G. *et al.* UBXD7 binds multiple ubiquitin ligases and implicates p97 in HIF1alpha turnover. *Cell* **134**, 804-816, doi:10.1016/j.cell.2008.06.048 (2008).

10 Wang, P. *et al.* UBXN1 interferes with Rig-I-like receptor-mediated antiviral immune response by targeting MAVS. *Cell Rep* **3**, 1057-1070, doi:10.1016/j.celrep.2013.02.027 (2013).

11 Kim, J. H. *et al.* FAS-associated factor-1 positively regulates type I interferon response to RNA virus infection by targeting NLRX1. *PLoS Pathog* **13**, e1006398, doi:10.1371/journal.ppat.1006398 (2017).

12 Dai, T. *et al.* FAF1 Regulates Antiviral Immunity by Inhibiting MAVS but Is Antagonized by Phosphorylation upon Viral Infection. *Cell Host Microbe* **24**, 776-790 e775, doi:10.1016/j.chom.2018.10.006 (2018).

13 Wang, Y. B. *et al.* Ubiquitin-associated Domain-containing UBX Protein UBXN1 is a Negative Regulator of NF-kappaB Signaling. *J Biol Chem*, doi:10.1074/jbc.M114.631689 (2015).

14 Hu, Y. *et al.* Multiple UBXN family members inhibit retrovirus and lentivirus production and canonical NFkappaBeta signaling by stabilizing IkappaBalpha. *PLoS Pathog* **13**, e1006187, doi:10.1371/journal.ppat.1006187 (2017).

15 Yang, L. *et al.* UBXN3B positively regulates STING-mediated antiviral immune responses. *Nat Commun* **9**, 2329, doi:10.1038/s41467-018-04759-8 (2018).

16 Silva, L. A. & Dermody, T. S. Chikungunya virus: epidemiology, replication, disease mechanisms, and prospective intervention strategies. *J Clin Invest* **127**, 737-749, doi:10.1172/JCI84417 (2017).

17 Lin, T. *et al.* CXCL10 Signaling Contributes to the Pathogenesis of Arthritogenic Alphaviruses. *Viruses* **12**, doi:10.3390/v12111252 (2020).

18 Harrison, A. G., Lin, T. & Wang, P. Mechanisms of SARS-CoV-2 Transmission and Pathogenesis. *Trends Immunol* **41**, 1100-1115, doi:10.1016/j.it.2020.10.004 (2020).

19 Sun, J. *et al.* Generation of a Broadly Useful Model for COVID-19 Pathogenesis, Vaccination, and Treatment. *Cell* **182**, 734-743 e735, doi:10.1016/j.cell.2020.06.010 (2020).

20 Hassan, A. O. *et al.* A SARS-CoV-2 Infection Model in Mice Demonstrates Protection by Neutralizing Antibodies. *Cell* **182**, 744-753 e744, doi:10.1016/j.cell.2020.06.011 (2020).

21 Chen, N. *et al.* Epidemiological and clinical characteristics of 99 cases of 2019 novel coronavirus pneumonia in Wuhan, China: a descriptive study. *The Lancet* **395**, 507–513, doi:https://doi.org/10.1016/S0140-6736(20)30211-7 (2020).

22 Guan, W.-j. *et al.* Clinical Characteristics of Coronavirus Disease 2019 in China *The New England Journal of Medicine* **382**, 1708-1720, doi:10.1056/NEJMoa2002032 (2020).

23 Imai, S. T. K. *et al.* Clinical characteristics of COVID-19 in 104 people with SARS-CoV-2 infection on the Diamond Princess cruise ship: a retrospective analysis. *Lancet Infectious Diseases* **20**, 1043-1050 (2020).

24 Zhang, J.-j. *et al.* Clinical characteristics of 140 patients infected with SARS-CoV-2 in Wuhan, China. *Allergy* **75**, 1730-1741, doi:10.1111/all.14238 (2020).

25 Zhang, B. *et al.* Clinical characteristics of 82 cases of death from COVID-19. *PLoS ONE* **15**, doi:https://doi.org/10.1371/journal.pone.0235458 (2020).

26 Liao, J. *et al.* Epidemiological and Clinical Characteristics of COVID-19 in Adolescents and Young Adults. *The Innovation* **1**, doi:10.1016/j.xinn.2020.04.001 (2020).

27 de Candia, P., Prattichizzo, F., Garavelli, S. & Matarese, G. T Cells: Warriors of SARS-CoV-2 Infection. *Trends Immunol* **42**, 18-30, doi:10.1016/j.it.2020.11.002 (2021).

28 Lee, J. N. *et al.* Identification of Ubxd8 protein as a sensor for unsaturated fatty acids and regulator of triglyceride synthesis. *Proc Natl Acad Sci U S A* **107**, 21424-21429, doi:10.1073/pnas.1011859107 (2010).

29 Olzmann, J. A., Richter, C. M. & Kopito, R. R. Spatial regulation of UBXD8 and p97/VCP controls ATGL-mediated lipid droplet turnover. *Proc Natl Acad Sci U S A* **110**, 1345-1350, doi:10.1073/pnas.1213738110 (2013).

30 Wang, C. W. & Lee, S. C. The ubiquitin-like (UBX)-domain-containing protein Ubx2/Ubxd8 regulates lipid droplet homeostasis. *Journal of cell science* **125**, 2930-2939, doi:10.1242/jcs.100230 (2012).

31 Kim, H. *et al.* UAS domain of Ubxd8 and FAF1 polymerizes upon interaction with long-chain unsaturated fatty acids. *Journal of lipid research* **54**, 2144-2152, doi:10.1194/jlr.M037218 (2013).

32 Imai, N. *et al.* Hepatocyte-Specific Depletion of UBXD8 Induces Periportal Steatosis in Mice Fed a High-Fat Diet. *PLoS One* **10**, e0127114, doi:10.1371/journal.pone.0127114 (2015).

33 Ohsaki, Y., Cheng, J., Fujita, A., Tokumoto, T. & Fujimoto, T. Cytoplasmic lipid droplets are sites of convergence of proteasomal and autophagic degradation of apolipoprotein B. *Mol Biol Cell* **17**, 2674-2683, doi:10.1091/mbc.e05-07-0659 (2006).

34 Ohsaki, Y., Cheng, J., Suzuki, M., Fujita, A. & Fujimoto, T. Lipid droplets are arrested in the ER membrane by tight binding of lipidated apolipoprotein B-100. *J Cell Sci* **121**, 2415-2422, doi:10.1242/jcs.025452 (2008).

35 Suzuki, M. *et al.* Derlin-1 and UBXD8 are engaged in dislocation and degradation of lipidated ApoB-100 at lipid droplets. *Mol Biol Cell* **23**, 800-810, doi:10.1091/mbc.E11-11-0950 (2012).

36 Xia, Y. *et al.* Pathogenic mutation of UBQLN2 impairs its interaction with UBXD8 and disrupts endoplasmic reticulum-associated protein degradation. *Journal of neurochemistry* **129**, 99-106, doi:10.1111/jnc.12606 (2014).

37 Phan, V. T. *et al.* The RasGAP proteins Ira2 and neurofibromin are negatively regulated by Gpb1 in yeast and ETEA in humans. *Mol Cell Biol* **30**, 2264-2279, doi:10.1128/mcb.01450-08 (2010).

38 Zhou, H. L., Geng, C., Luo, G. & Lou, H. The p97-UBXD8 complex destabilizes mRNA by promoting release of ubiquitinated HuR from mRNP. *Genes & development* **27**, 1046-1058, doi:10.1101/gad.215681.113 (2013).

39 Glinka, T. *et al.* Signal-peptide-mediated translocation is regulated by a p97-AIRAPL complex. *The Biochemical journal* **457**, 253-261, doi:10.1042/bj20130710 (2014).

40 Geng, T. *et al.* A critical role for STING signaling in limiting pathogenesis of Chikungunya virus. *J Infect Dis*, doi:10.1093/infdis/jiaa694 (2020).

41 McGuckin Wuertz, K. *et al.* STING is required for host defense against neuropathological West Nile virus infection. *PLoS Pathog* **15**, e1007899, doi:10.1371/journal.ppat.1007899 (2019).

42 Zidar, D. A. *et al.* Association of Lymphopenia With Risk of Mortality Among Adults in the US General Population. *JAMA Netw Open* **2**, e1916526, doi:10.1001/jamanetworkopen.2019.16526 (2019).

43 Conley, M. E. *et al.* Primary B cell immunodeficiencies: comparisons and contrasts. *Annu Rev Immunol* **27**, 199-227, doi:10.1146/annurev.immunol.021908.132649 (2009).

44 Yong, P. F., Thaventhiran, J. E. & Grimbacher, B. "A rose is a rose is a rose," but CVID is Not CVID common variable immune deficiency (CVID), what do we know in 2011? *Adv Immunol* **111**, 47-107, doi:10.1016/B978-0-12-385991-4.00002-7 (2011).

45 Chang, A. Y. *et al.* Chikungunya Arthritis Mechanisms in the Americas: A Cross-Sectional Analysis of Chikungunya Arthritis Patients Twenty-Two Months After Infection Demonstrating No Detectable Viral Persistence in Synovial Fluid. *Arthritis Rheumatol* **70**, 585-593, doi:10.1002/art.40383 (2018).

46 He, X. *et al.* Temporal dynamics in viral shedding and transmissibility of COVID-19. *Nat Med* **26**, 672-675, doi:10.1038/s41591-020-0869-5 (2020).

47 Liu, J. *et al.* Neutrophil-to-lymphocyte ratio predicts critical illness patients with 2019 coronavirus disease in the early stage. *J Transl Med* **18**, 206, doi:10.1186/s12967-020-02374-0 (2020).

48 Guo, X. *et al.* Neutrophil:lymphocyte ratio is positively related to type 2 diabetes in a large-scale adult population: a Tianjin Chronic Low-Grade Systemic Inflammation and Health cohort study. *Eur J Endocrinol* **173**, 217-225, doi:10.1530/EJE-15-0176 (2015).

49 Angkananard, T., Anothaisintawee, T., McEvoy, M., Attia, J. & Thakkinstian, A. Neutrophil Lymphocyte Ratio and Cardiovascular Disease Risk: A Systematic Review and Meta-Analysis. *Biomed Res Int* **2018**, 2703518, doi:10.1155/2018/2703518 (2018).

50 Li, J. *et al.* Neutrophil-to-Lymphocyte Ratio Positively Correlates to Age in Healthy Population. *J Clin Lab Anal* **29**, 437-443, doi:10.1002/jcla.21791 (2015).

51 Schwantes-An, T. H. *et al.* Genome-wide association study and meta-analysis on alcohol-related liver cirrhosis identifies novel genetic risk factors. *Hepatology*, doi:10.1002/hep.31535 (2020).

52 Gorchakov, R. *et al.* Attenuation of Chikungunya virus vaccine strain 181/clone 25 is determined by two amino acid substitutions in the E2 envelope glycoprotein. *J Virol* **86**, 6084-6096, doi:10.1128/JVI.06449-11 (2012).

53 Tretyakova, I., Hearn, J., Wang, E., Weaver, S. & Pushko, P. DNA vaccine initiates replication of live attenuated chikungunya virus in vitro and elicits protective immune response in mice. *J Infect Dis* **209**, 1882-1890, doi:10.1093/infdis/jiu114 (2014).

54 Wang, P. *et al.* Caspase-12 controls West Nile virus infection via the viral RNA receptor RIG-I. *Nat Immunol* **11**, 912-919, doi:10.1038/ni.1933 (2010).

55 Yang, L. *et al.* Macrophage scavenger receptor 1 controls Chikungunya virus infection through autophagy in mice. *Commun Biol* **3**, 556, doi:10.1038/s42003-020-01285-6 (2020).

FIGURE LEGEND

Fig.1 UBXN3B is essential for controlling SARS-CoV-2 and influenza pathogenesis. **a-d**) Sex-and-age matched mice were administered $2x10^5$ plaque forming units (PFU) of SARS-CoV-2 intranasally. **a**) Percentage changes in the body mass of mock-treated Cre^+ $Ubxn3b^{flox/flox}$ (designated *Ubxn3b*$^{+/+}$) and tamoxifen (TMX) -treated Cre^+ $Ubxn3b^{flox/flox}$ (designated *Ubxn3b*$^{-/-}$) littermates, during the course of SARS-CoV-2 infection. Data point: mean ± s.e.m, N=6-8. *, p<0.05; **, p<0.01; ***, p<0.001 (two-tailed Student's *t*-test). **b**) Representative micrographs of hematoxylin and eosin staining (H&E) of lung sections from mock or SARS-CoV-2 infected mice on day 3 and 10 post infection (p.i.). The green arrow points to a cluster of immune infiltrates. The red arrow indicates a cluster of brownish cells of hemosiderosis. Magnification 400 x. **c**) Iron-staining (blue) of lung sections from mock or SARS-CoV-2 infected mice on days 3 and 10 p.i. Black arrows point to iron laden cells. Mock: mock infected. N=2 (mock), 4 (Day 3), 7 (Day 10), 3 (Day 35) per genotype. **e, f**) Sex-and-age matched mice were administered 350 $CCID_{50}$ (cell culture infectious dose 50% assay) influenza A PR/8/34 H1N1 intranasally. **e**) The percentage of the body mass relative to day 0 (weighed immediately before infection). Data point: mean ± s.e.m. N= 5-6. **f**) The survival curve. N=6 per genotype. P=0.02 (Log-Rank test).

Fig.2 UBXN3B is essential for controlling SARS-CoV-2 pathogenesis. Sex-and-age matched mice were administered $2x10^5$ plaque forming units (PFU) of SARS-CoV-2 intranasally. **a**) Quantitative RT-PCR (qPCR) quantification of SARS-CoV-2 loads in the lung on days 3 and 10 post infection (p.i). Data point: mean ± s.e.m, N=8 per group for day 3 and 6 for day 10. **b**) Quantification of serum immune mediators by multiplex ELISA during the course of SARS-CoV-2 infection. Each symbol= one mouse, the small horizontal line: the median of the result. *,

P<0.05; **, P<0.01 (non-parametric Mann-Whitney test) between *Ubxn3b*$^{+/+}$ and *Ubxn3b*$^{-/-}$ littermates at the same time point.

Fig.3 UBXN3B is essential for immune cell homeostasis during SARS-CoV-2 infection. Sex-and-age matched mice were administered 2x10^5 plaque forming units (PFU) of SARS-CoV-2 intranasally. **a**) The total CD45$^+$ cells, **b**) the percentage (relative to CD45$^+$ cells) of various immune cell populations quantified by FACS, **c**) the neutrophil-to-T cell ratio, in one lung of SARS-CoV-2 infected mice on day 3 post infection (p.i.). **d**) The percentage (relative to CD45$^+$ cells) of various immune cell populations, and **e**) the neutrophil-to-B/T cell ratios (N/B, N/T), in the blood on day 3 post infection (p.i.). The cell counts and percentage of various immune cell populations **f**) and **g**) the neutrophil-to-B/T cell ratios in one lung, **h**) cell counts in the blood on day 35 p.i. Neu: neutrophil, Mac/Mono: macrophage/monocyte, DC: dendritic cell. Each symbol=one mouse. *, p<0.05; **, p<0.01; ***, p<0.001 (non-parametric Mann-Whitney test). The horizontal line indicates the median of the result.

Fig.4 UBXN3B is essential for restricting pathogenesis of CHIKV arthritis. Sex-and-age matched littermates were administered 1 x 10^5 plaque forming units (PFU) of CHIKV subcutaneously in one footpad. **a**) Representative images of foot swelling (n=3 animals). The red arrows indicate the foot inoculated with CHIKV. **b**) Fold changes in the footpad dimensions of infected mice over uninfected (day 0). Data point: mean ± s.e.m (n = 3 mice per genotype). **c**) Representative micrographs of hematoxylin and eosin staining of ankle joints on day 16 post CHIKV infection (p.i.) [N = 10 *Ubxn3b*$^{+/+}$, 5 *Ubxn3b*$^{-/-}$animals]. B: bone, T: tendon, M: muscle. Magnification: 200 x. **d**) The arbitrary scores of ankle joint inflammation and damage using scales of 1 to 5, with 5 representing the worst disease presentation. **e**)The percentage (relative to CD45$^+$ cells) of various immune cell populations quantified by FACS, and **f**) the neutrophil to B/T cell ratios, in the CHIKV-inoculated footpad, the spleen and blood circulation on day 7 post

672 infection (p.i.). Neu: neutrophil, Mac/Mono: macrophage/monocyte, DC: dendritic cell. Each
673 symbol=one mouse. The horizontal line indicates the median of the result. *, p<0.05; **, p<0.01;
674 ***, p<0.001 (two-tailed Student's t-test for panel **b**, **d**; non-parametric Mann-Whitney test for
675 panel **e**, **f**).
676
677 **Fig.5 UBXN3B is essential for steady-state immune cell homeostasis.** The percentage
678 (relative to $CD45^+$ cells) of various immune cell populations, cell counts, and the neutrophil to
679 B/T cell ratios, were quantified by FACS in the **a**) blood and **b**) spleen of specific pathogen-free
680 mice. Neu: neutrophil, Mac/Mono: macrophage/monocyte, DC: dendritic cell, Mast: mast cell,
681 Eos: eosinophil, NK: natural killer, NKT: natural killer T cells. Each symbol=one mouse. The
682 horizontal line indicates the median of the result. *, p<0.05; **, p<0.01; ***, p<0.001 (two-tailed
683 Student's t-test).
684
685 **Fig.6 UBXN3B is essential for hematopoietic hemostasis.** The **a**) gating strategy and **b**)
686 frequencies (relative to live cells after lysis of red blood cells) of various mature immune cells,
687 the **c**) gating plan and **d**) frequencies of stem cells/progenitors, in the bone marrows of specific
688 pathogen-free mice. BM: bone marrow, Neu: neutrophil, Mono: monocyte, DC: dendritic cell, NK:
689 natural killer, LSK: Lin^- Sca^+ Kit^+, LT-HSC: long-term hematopoietic stem cell, ST-HSC: short-
690 term multipotent HSC (also known as MPP), CMP: common myeloid progenitor, CLP: common
691 lymphoid progenitor, GMP: granulocyte–macrophage progenitor, MEP: megakaryocyte–
692 erythroid progenitor, ProB: progenitor B, PreB: precursor B, ImmB: immature B. Each
693 symbol=one mouse. The horizontal line indicates the median of the result. *, p<0.05; **, p<0.01;
694 ***, p<0.001 (two-tailed Student's t-test).
695
696 **Supplemental Materials**
697 Supplemental Fig. 1-6

698 Supplemental Movie 1: SARS-CoV-2-infected *Ubxn3b*$^{+/+}$ mice on day 2 after infection.
699
700 Supplemental Movie 2: SARS-CoV-2-infected *Ubxn3b*$^{-/-}$ mice on day 2 after infection.
701

Fig.1

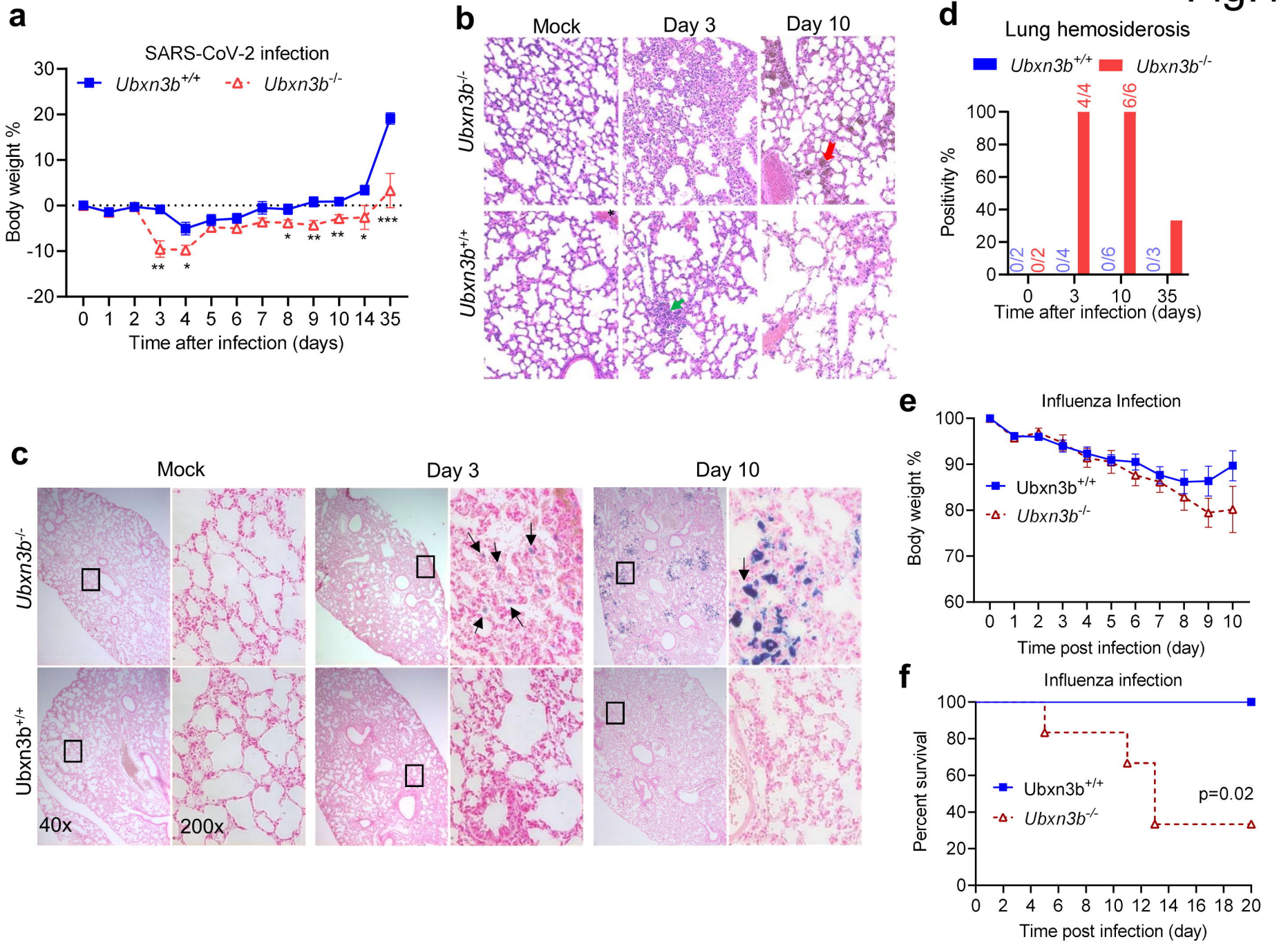
a
SARS-CoV-2 infection
Ubxn3b+/+
Ubxn3b-/-
Body weight %
Time after infection (days)
b
Mock
Day 3
Day 10
Ubxn3b-/-
Ubxn3b+/+
d
Lung hemosiderosis
Ubxn3b+/+
Ubxn3b-/-
Positivity %
0/2
0/2
0/4
4/4
0/6
6/6
0/3
Time after infection (days)
c
Mock
Day 3
Day 10
Ubxn3b-/-
Ubxn3b+/+
40x
200x
e
Influenza Infection
Body weight %
Ubxn3b+/+
Ubxn3b-/-
Time post infection (day)
f
Influenza infection
Percent survival
Ubxn3b+/+
Ubxn3b-/-
p=0.02
Time post infection (day)

Fig.2

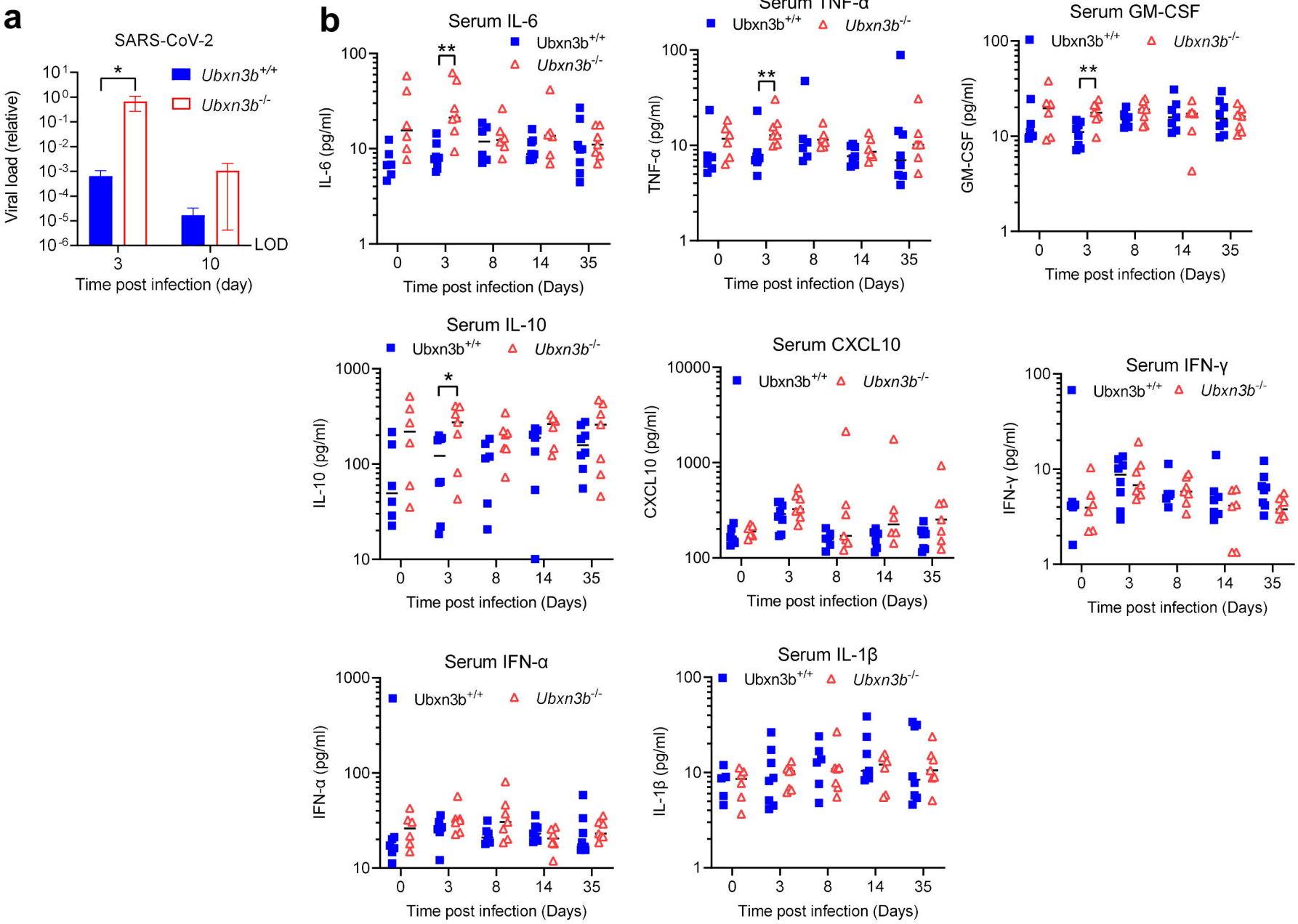
a
SARS-CoV-2
Viral load (relative)
Ubxn3b+/+
Ubxn3b-/-
LOD
Time post infection (day)
b
Serum IL-6
IL-6 (pg/ml)
Serum TNF-α
TNF-α (pg/ml)
Serum GM-CSF
GM-CSF (pg/ml)
Serum IL-10
IL-10 (pg/ml)
Serum CXCL10
CXCL10 (pg/ml)
Serum IFN-γ
IFN-γ (pg/ml)
Serum IFN-α
IFN-α (pg/ml)
Serum IL-1β
IL-1β (pg/ml)
Time post infection (Days)

Fig.3

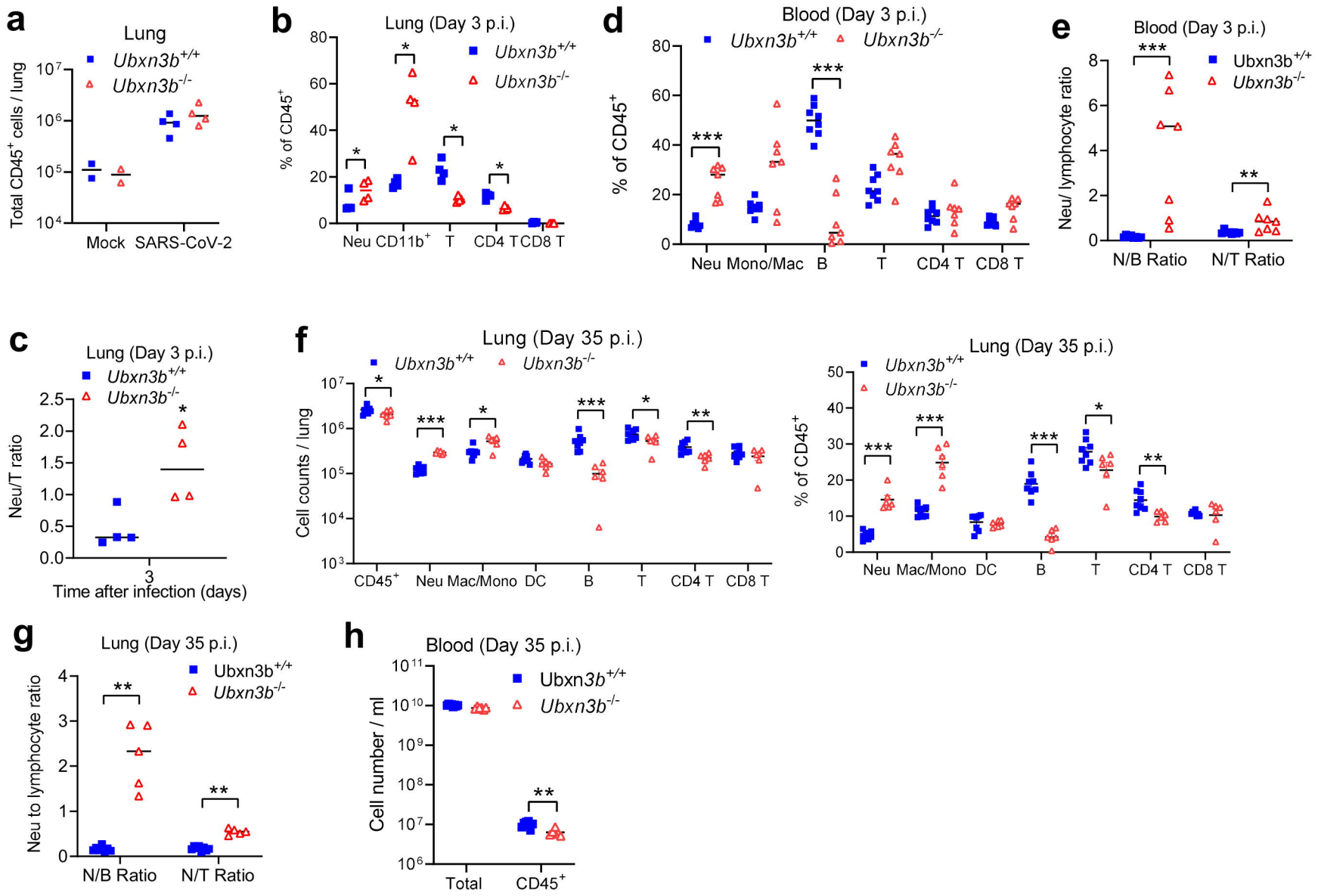
a
Lung
Ubxn3b+/+
Ubxn3b-/-
Total CD45+ cells / lung
Mock
SARS-CoV-2
b
Lung (Day 3 p.i.)
% of CD45+
Neu
CD11b+
T
CD4 T
CD8 T
d
Blood (Day 3 p.i.)
Mono/Mac
B
e
Neu/ lymphocyte ratio
N/B Ratio
N/T Ratio
c
Neu/T ratio
Time after infection (days)
f
Lung (Day 35 p.i.)
Cell counts / lung
CD45+
Mac/Mono
DC
g
Neu to lymphocyte ratio
h
Blood (Day 35 p.i.)
Cell number / ml
Total

Fig.4

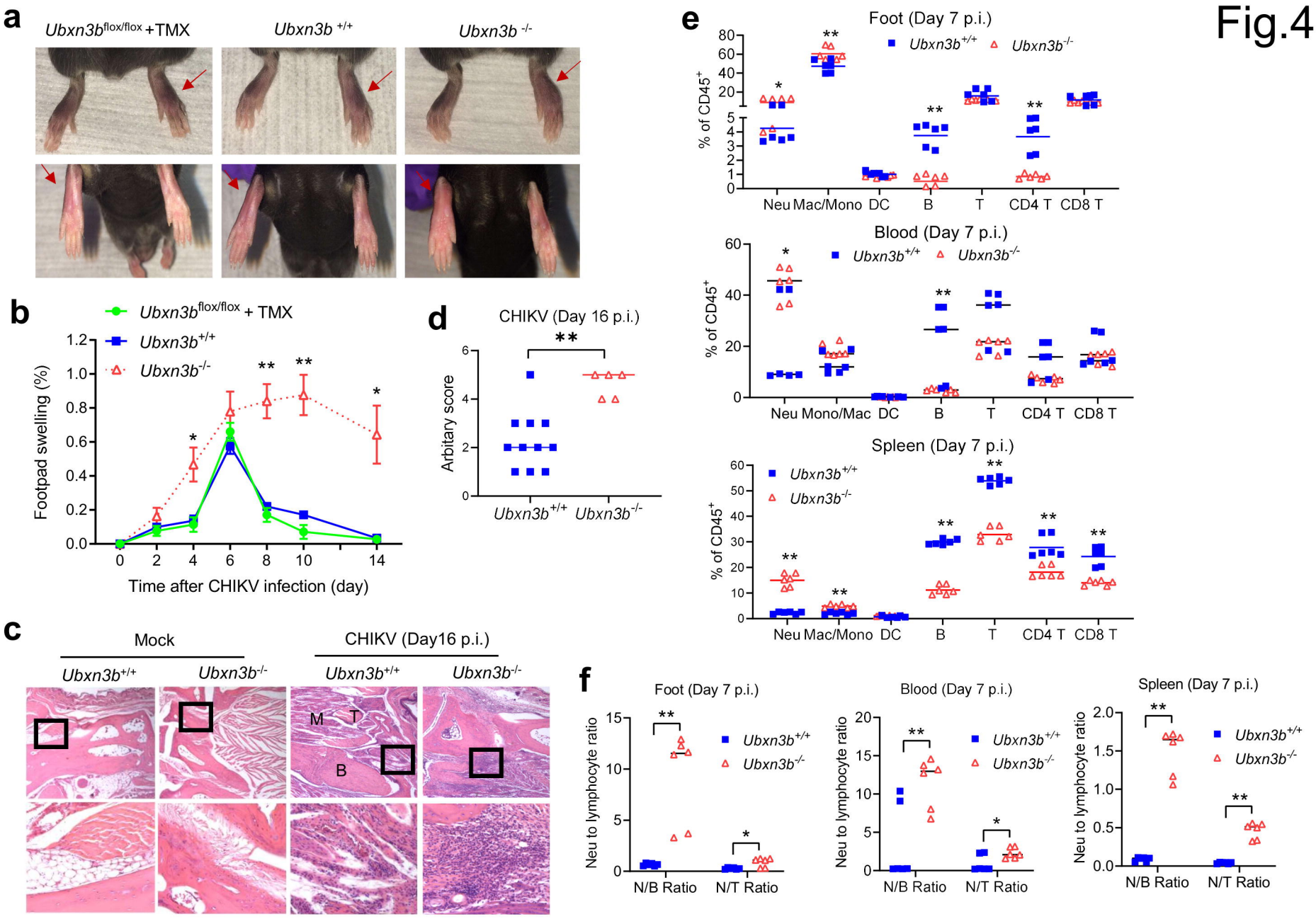
a
Ubxn3b flox/flox +TMX
Ubxn3b +/+
Ubxn3b -/-
b
Ubxn3b flox/flox + TMX
Ubxn3b +/+
Ubxn3b -/-
Footpad swelling (%)
Time after CHIKV infection (day)
d
CHIKV (Day 16 p.i.)
Arbitary score
e
Foot (Day 7 p.i.)
Blood (Day 7 p.i.)
Spleen (Day 7 p.i.)
% of CD45+
Neu Mac/Mono DC B T CD4 T CD8 T
Neu Mono/Mac DC B T CD4 T CD8 T
c
Mock
CHIKV (Day16 p.i.)
M
T
B
f
Foot (Day 7 p.i.)
Blood (Day 7 p.i.)
Spleen (Day 7 p.i.)
Neu to lymphocyte ratio
N/B Ratio
N/T Ratio

Fig.5

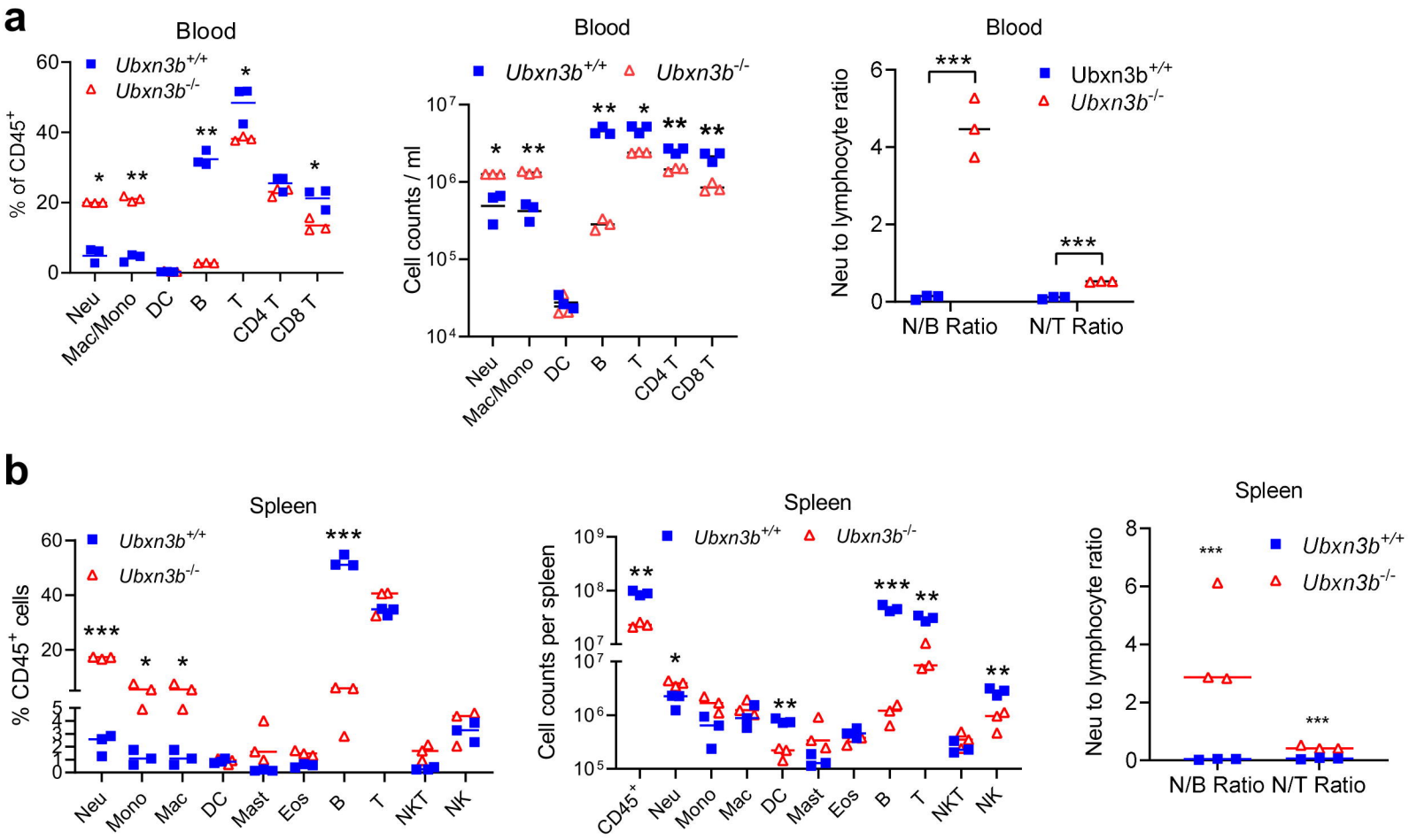
a
Blood
Ubxn3b+/+
Ubxn3b-/-
% of CD45+
Neu
Mac/Mono
DC
B
T
CD4 T
CD8 T
Blood
Cell counts / ml
Blood
Neu to lymphocyte ratio
N/B Ratio
N/T Ratio
b
Spleen
% CD45+ cells
Mono
Mac
Mast
Eos
NKT
NK
Spleen
Cell counts per spleen
CD45+
Spleen
Neu to lymphocyte ratio

Fig.6

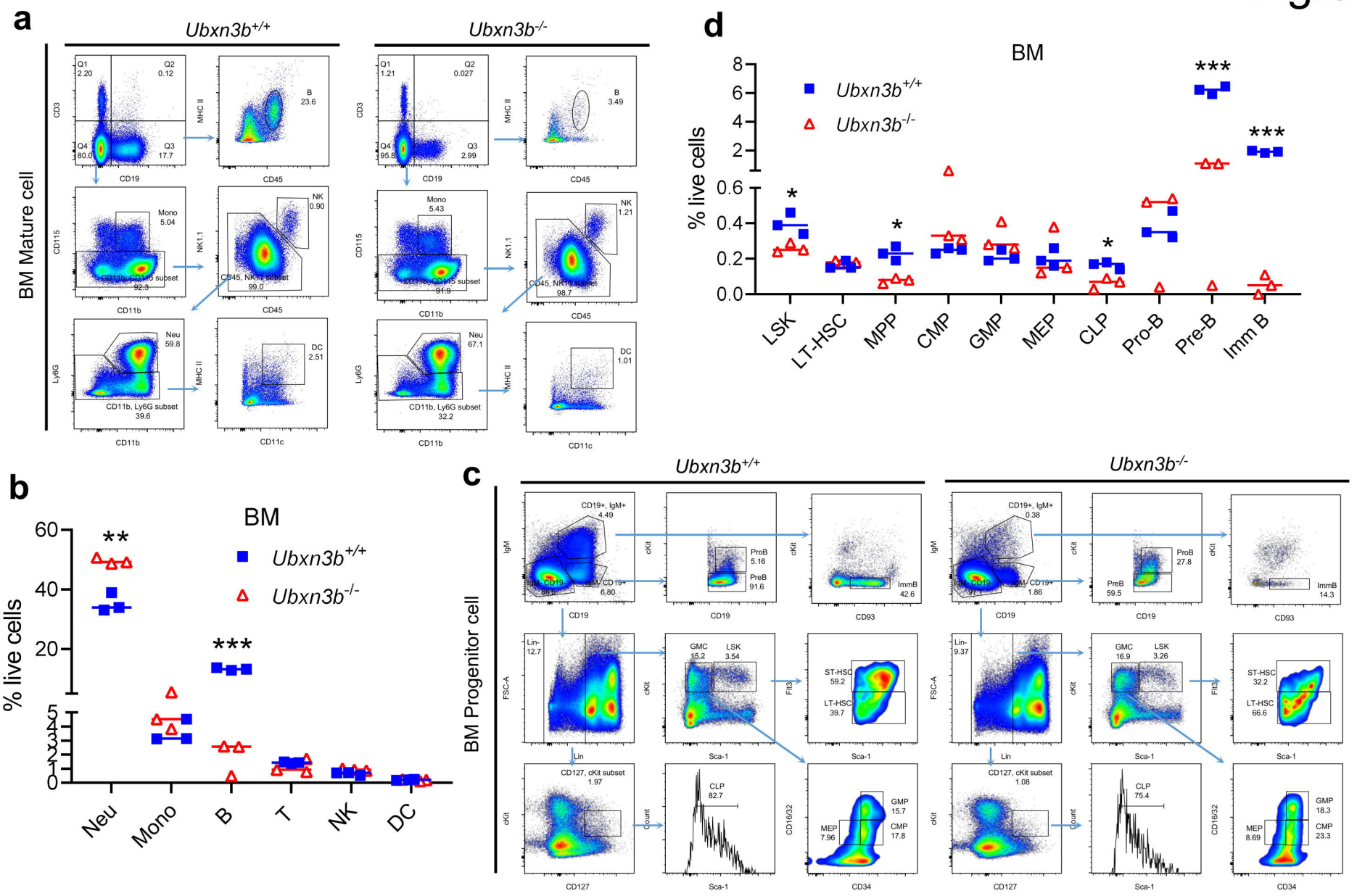
a
Ubxn3b+/+
Ubxn3b-/-
BM Mature cell
CD3
CD19
MHC II
CD45
CD115
CD11b
NK1.1
Ly6G
CD11c
b
BM
Ubxn3b+/+
Ubxn3b-/-
% live cells
Neu
Mono
B
T
NK
DC
c
Ubxn3b+/+
Ubxn3b-/-
BM Progenitor cell
IgM
cKit
CD93
Lin-
FSC-A
Sca-1
Flt3
CD127
CD16/32
CD34
Count
ProB
PreB
ImmB
ST-HSC
LT-HSC
GMC
LSK
CLP
GMP
MEP
CMP
d
BM
Ubxn3b+/+
Ubxn3b-/-
% live cells
LSK
LT-HSC
MPP
CMP
GMP
MEP
CLP
Pro-B
Pre-B
Imm B